Volume 9
Number 36
28 September 2021
Pages 20081–20818

Journal of Materials Chemistry A

Materials for energy and sustainability

rsc.li/materials-a

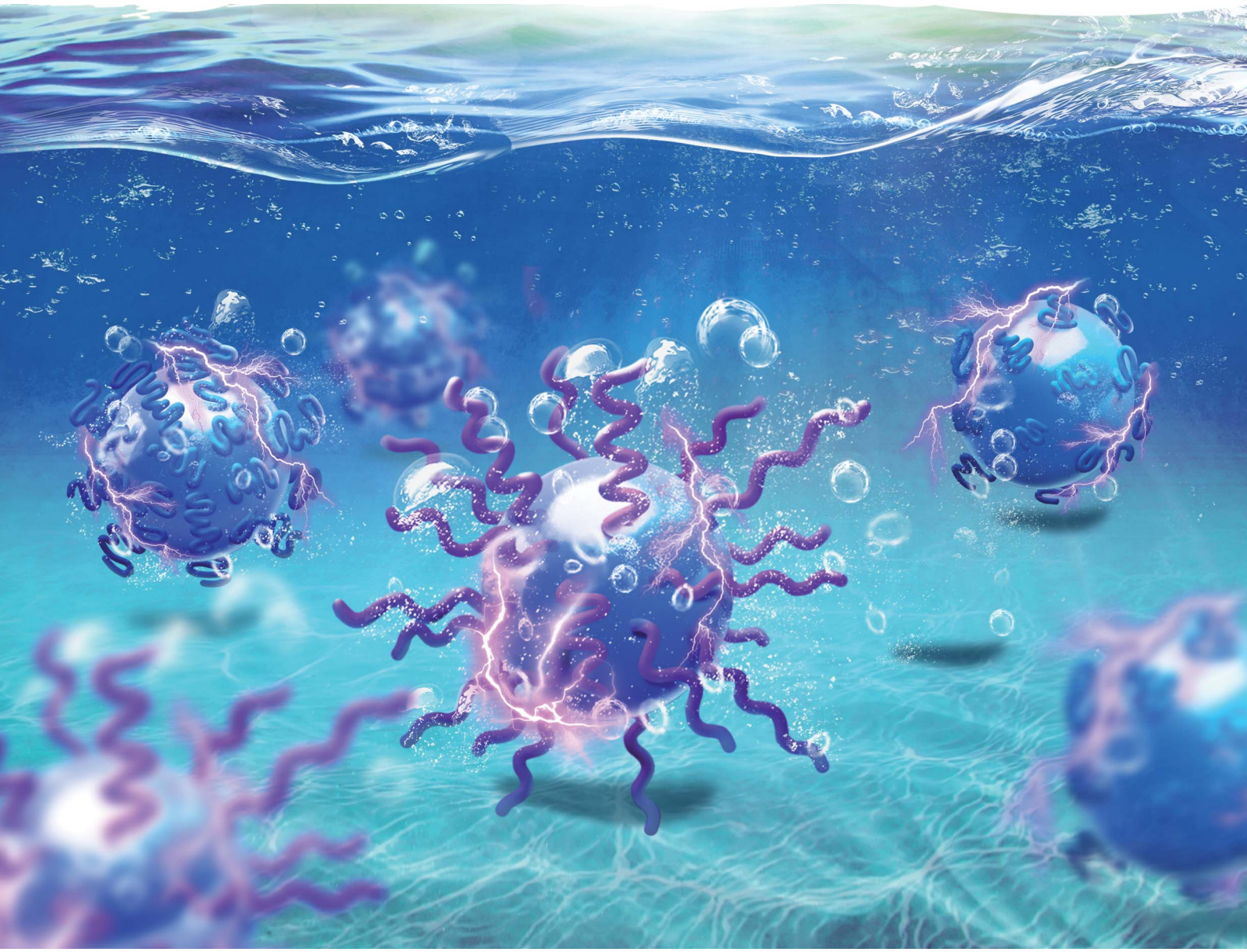

ISSN 2050-7488

ROYAL SOCIETY OF CHEMISTRY

PAPER

Zhiqun Lin *et al.*

Tailoring oxygen evolution reaction activity of metal-oxide spinel nanoparticles *via* judiciously regulating surface-capping polymers

Journal of Materials Chemistry A

ROYAL SOCIETY OF CHEMISTRY

PAPER

View Article Online
View Journal | View Issue

Cite this: J. Mater. Chem. A, 2021, 9, 20375

Tailoring oxygen evolution reaction activity of metal-oxide spinel nanoparticles *via* judiciously regulating surface-capping polymers†

Christopher D. Sewell, Zewei Wang, Yeu-Wei Harn, Shuang Liang, Likun Gao, Xun Cui and Zhiqun Lin *

High cost and scarcity of the state-of-the-art noble metal-based catalysts represents one of the critical hurdles to be overcome in electrocatalysis. A promising direction is to utilize transition metal-based nanoparticles (NPs), which offer superior electrocatalytic performance over their bulk counterparts. Capping the surface of NPs with polymers is widely recognized as an effective means towards their dispersion and stabilization. However, it is often circumvented due to its tendency to lower the electrocatalytic activity of the ligated NPs. Here, we report the *first* systematic investigation into the impact of the chain density and hydrophilicity of the surface-capping polymers, which can be judiciously regulated, on the oxygen evolution reaction (OER) activity. By capitalizing on star-like diblock copolymers as nanoreactors, spinel $CoFe_2O_4$ (CFO) NPs permanently ligated with polymers of interest (*i.e.*, varied chain density and characteristic) are crafted. The correlation between the chain density and hydrophilicity of surface-capping polymers and the OER activity of CFO NPs are scrutinized. Intriguingly, decreasing the number of surface-capping chains and increasing the chain hydrophilicity result in significantly decreased overpotential, caused by an increased exposure of the active material (CFO) to the electrolyte and reduced diffusion resistance. This study provides insight into the strategies for mitigating the activity-limiting properties of surface polymers and tailoring the electrocatalytic properties of polymer-ligated NPs.

Received 28th May 2021
Accepted 21st July 2021

DOI: 10.1039/d1ta04511c

rsc.li/materials-a

1. Introduction

Fuel cells, metal–air batteries, and water splitting devices are widely recognized as promising next-generation energy conversion and storage techniques which have the potential to cost-effectively meet the energy storage demands required to enable the practical use of renewable energy sources.[1–4] The performance of the energy conversion and storage techniques is limited by the sluggish kinetics of the oxygen evolution reaction (OER) and oxygen reduction reaction (ORR),[5–8] necessitating expensive noble-metal based electrocatalysts, such as IrO_2 and RuO_2 for OER, which limit the potential for large-scale applications because of their high cost and earth scarcity.[9,10] In this context, a significant amount of research has focused on developing alternative electrocatalysts utilizing cheaper, more naturally abundant transition metals.[11–14] Transition metal-oxide-based catalysts offer additional advantages such as tunability, with structures such as perovskites and spinels allowing a large diversity of metal compositions, and high stability in alkaline media.[15,16] Spinel ferrites, MFe_2O_4 (M = Co, Ni, *etc.*), are of particular interest as OER electrocatalysts due to their promising catalytic activity, natural abundance, and low cost.[17] The high OER performance of spinel ferrites can be attributed to their mixed valence, tunability and excellent redox stability.[18] Numerous studies have employed nanomaterials to increase the performance of transition metal-based electrocatalysts due to their increased specific surface area, increased active site density, tunable binding energy to intermediates, *etc.*13,16,19,20

One issue facing the use of nanoparticles (NPs) is their tendency to aggregate into larger clusters, deteriorating electrocatalytic performance due to reduced active surface area.[21–24] In order to ensure the widespread application of next-generation energy storage and conversion technologies, it is imperative that electrocatalysts exhibit high stability under harsh reaction conditions.[25] Therefore, nanomaterial catalysts have to incorporate some form of particle stabilization to retain desirable activity.[26,27] The most commonly employed strategy is to anchor NPs onto or embed them in between highly conductive substrates, such as reduced graphene oxide, carbon nanotubes, and 2D MXenes.[28–32] Coating nanomaterials with thin layers of graphene has also been successfully employed to improve stability during electrocatalysis.[33] These methods

School of Materials Science and Engineering, Georgia Institute of Technology, Atlanta, Georgia, 30332, USA. E-mail: Zhiqun.lin@mse.gatech.edu

† Electronic supplementary information (ESI) available. See DOI: 10.1039/d1ta04511c

provide the additional advantage of increased system conductivity, which promotes higher electrocatalytic activity. Another, much less often utilized, stabilization strategy is to cap NPs with ligands.[34–37] Ligands are highly effective at stabilizing NPs and yielding higher uniformity, but reduce the activity of the electrocatalyst materials.[38,39] Typically, NPs are formed using surface capping ligands, which decrease surface energy and prevent direct contact with other NPs, thereby preventing agglomeration.[40,41] While an effective route to NP stabilization, the use of long ligands as capping agents is largely avoided in electrocatalysis because of the surface area-dependent nature of the process. If utilized during NP formation, surface ligands are typically removed to achieve higher performance because they reduce the amount of exposed active sites and can block the access of reactants to the NP surface.[41–43] Despite having potential as a viable stabilization strategy, there has been little research regarding the impact of long surface ligands and their properties on the activity of electrocatalytic materials.

Herein, we report on crafting polymer-ligated metal-oxide spinel NPs *via* capitalizing on rationally designed star-like block copolymers as nanoreactors, and subsequently conducting the *first systematic* investigation into the impact of composition (and by extension, hydrophilicity) and grafting density of the surface-capping polymers on OER activity. First, a series of star-like diblock copolymers (*i.e.*, 8-arm and 21-arm poly(acrylic acid)-*block*-polystyrene (PAA-*b*-PS), 21-arm poly(acrylic acid)-*block*-poly(ethylene oxide) (PAA-*b*-PEO)) with well-defined molecular weights (MWs) and low polydispersity index (PDI) are successfully synthesized. Afterwards, they are exploited as nanoreactors for the growth of spinel $CoFe_2O_4$ (CFO) NPs with comparable size and controlled surface chemistry. Notably, the outer blocks (*i.e.*, PS and PEO) of star-like block polymers are covalently linked to the inner PAA blocks, resulting in permanently attached polymer chains on the surface of CFO NP without dynamic ligand dissociation. Our unconventional strategy to yield CFO NPs renders subsequent exploration of the effect of NP surface chemistry on their electrocatalytic performance in different aspects, namely, the hydrophilicity (PS *vs.* PEO) and chain-density (8 arms *vs.* 21 arms) of surface-capping polymers. In-depth study on the electrochemical and electrocatalytic properties of these hairy CFO NPs reveals that reducing diffusion resistance and increasing the exposure of the active material to electrolyte have the largest positive impact on the OER activity. These observations correlate well with both a decrease in the number of surface-capping polymers and increase in the outer-block chain hydrophilicity. CFO NPs permanently ligated with 21 PEO chains were found to exhibit the highest OER activity, requiring an overpotential at 10 mA cm^{-2} (η_{10}) of 409 mV; this performance is similar to or slightly better than that achieved in studies utilizing comparable CFO-based systems.[17] Several works have already developed CFO-based electrocatalysts with significantly enhanced improvement, some even surpassing commercial IrO_2 and RuO_2.[17,18,44,45] However, to produce such high electrocatalytic activities, these studies typically utilize more complex catalyst systems involving dopants, defect engineering, architectured porous structures, or improved substrates. This study avoids the use of these well-known strategies to improve the OER performance of spinel oxides with the intention of limiting the complexity of the catalyst system to enable a more systematic investigation into the effect of surface-capping polymers on OER performance. The findings in our study signify that the negative impact of surface-capping polymers on electrocatalysts can be reduced by tuning the polymer properties; by mitigating this negative impact, capping the surface of NPs with polymers could have the potential to be effectively utilized as a stabilization method in electrocatalysis.

2. Results and discussion

2.1 Synthesis of polymer-ligated CFO NPs

A star-like macroinitiator, 21-Br-β-CD, was synthesized by converting 21 hydroxyl groups of β-CD to bromine groups *via* esterification (Scheme 1a, step 1). Based on proton nuclear magnetic resonance (^{1}H-NMR) (Fig. S3†), nearly 100% conversion from hydroxyl groups to bromide terminals was achieved.[46] Afterwards, the 21-Br-β-CD was utilized as a macroinitiator for the sequential atom transfer radical polymerization (ATRP) of *tert*-butyl acrylate (*t*BA) and Styrene (St) monomers, respectively, to synthesize 21-arm, star-like P*t*BA-*b*-PS diblock copolymers (Scheme 1a, step 2 and 1b, step 3). As shown in Fig. S4,† the as-prepared star-like P*t*BA and P*t*BA-*b*-PS possessed monomodal traces in gel permeation chromatography (GPC) and narrow MW distributions (*i.e.* PDI <1.2), indicating the absence of intermolecular coupling during ATRP reactions.[46,47] Following hydrolysis with trifluoroacetic acid (TFA) (Scheme 1b, step 4), the hydrophobic P*t*BA-*b*-PS was successfully converted into amphiphilic PAA-*b*-PS (upper right panel; Scheme 1b).[46]

It is notable that the bromine terminal of the 21-arm, star-like P*t*BA can be readily substituted by S_N2 reaction with sodium azide to facilitate the click chemistry for grafting additional polymer blocks. As illustrated in Fig. S5,† the appearance of a new peak in the Fourier transform infrared (FT-IR) spectra around 2100 cm^{-1}, which is characteristic of the stretching mode of azide groups, suggests the successful substitution of bromine with azide group.[48] Subsequently, alkyne-terminated PEO, synthesized in accordance with the previous report,[48] was successfully clicked onto azide-terminated P*t*BA *via* a copper(I)-catalyzed alkyne–azide click cycloaddition reaction (Scheme 1c, step 3), as evidenced by FT-IR and GPC (Fig. S5 and S6†).[47] Hydrolyzing the inner P*t*BA (Scheme 1c, step 4) with TFA in chloroform of the as-prepared P*t*BA-*b*-PEO resulted in the formation of 21-arm, star-like PAA-*b*-PEO (upper right panel; Scheme 1c).

By replacing the 21-arm β-CD with 4-*tert*-butylcalix [8] arene (4tBC8A), 8-Br-4tBC8A was successfully prepared *via* substitution of the 8 hydroxyl groups with bromine terminals (Scheme 1d, step 1; also see *Experimental section*), as verified by ^{1}H-NMR (Fig. S7†). Afterwards, the as-prepared 8-Br-4tBC8A was used as a macroinitiator for the sequential ATRP of *t*BA and St for the synthesis of 8-arm, star-like PtBA-*b*-PS (Scheme 1d, steps 2–3), followed by hydrolysis to yield 8-arm, star-like PAA-*b*-PS, which is similar to the synthesis of 21-arm, star-like PAA-*b*-PS as noted above. Corresponding GPC curves can be seen in Fig. S8.† The

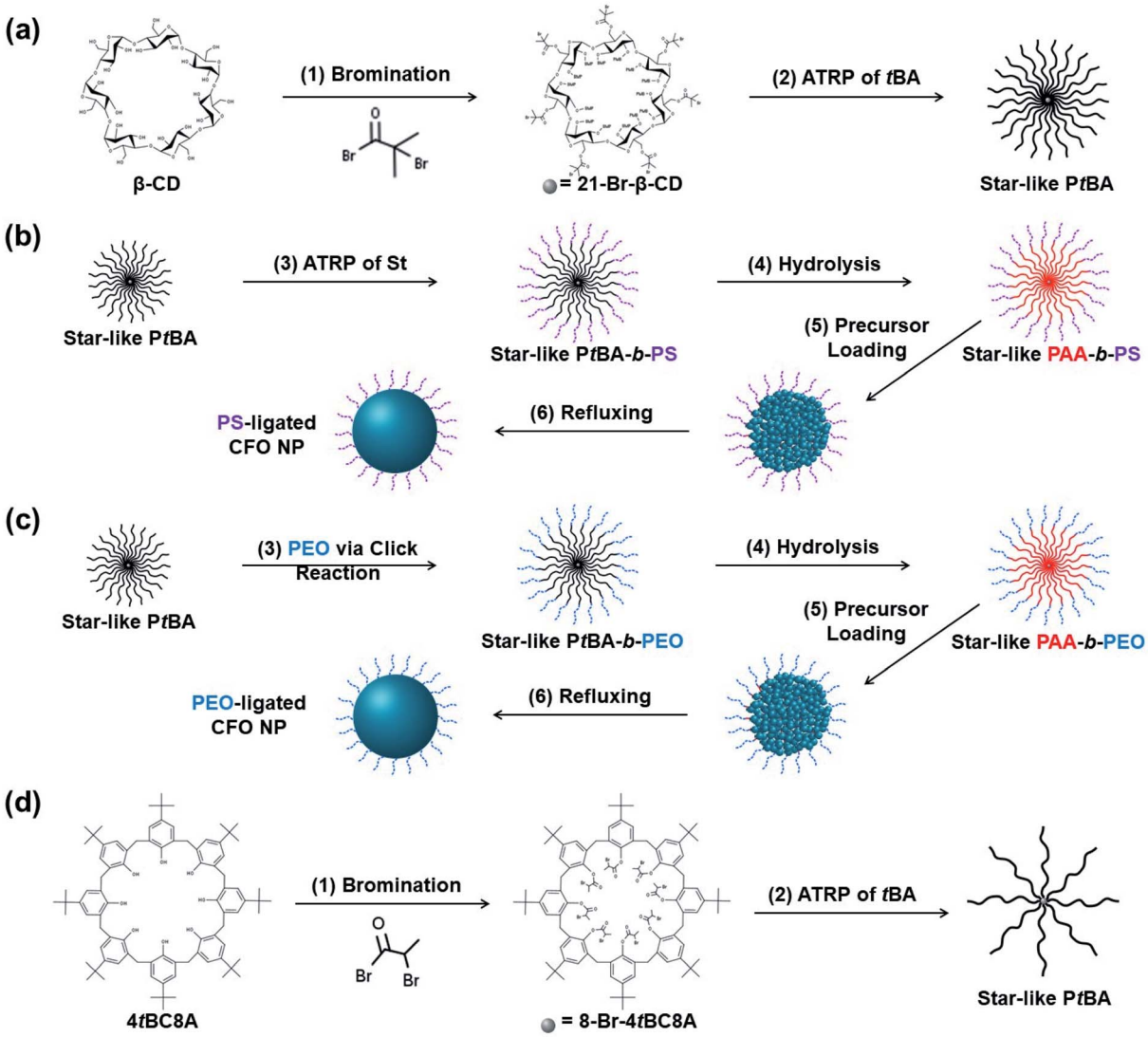

Scheme 1 Schematic representation of synthesis route to (a) 21-arm, star-like PtBA, (b) PS-ligated $CoFe_2O_4$ (CFO) NPs, (c) PEO-ligated CFO NPs, and (d) 8-arm, star-like PtBA.

MWs and PDI of as-prepared star-like diblock copolymer nanoreactors are summarized in Table S1.†

Subsequently, the as-prepared star-like diblock copolymers were utilized as nanoreactors for the synthesis of polymer-ligated CFO NPs (Scheme 1b and c, steps 5–6).[49] Typically, the synthesis procedure for the formation of CFO NPs remains consistent regardless of the star-like diblock copolymer nanoreactors used. Specifically, the nanoreactors were first dissolved in the mixture of diphenyl ether (DPE) and benzyl alcohol (BA) (DPE : BA = 9 : 1 by volume) to form unimolecular, stable spherical micelles[50] (see *Experimental section*). In the solvent mixture, using the star-like PAA-*b*-PS as an example, the DPE is the primary solvent, acting as a good solvent for the PS outer-blocks and a poor solvent for the PAA inner-blocks. Since the PAA chains are partially collapsed in this solvent, BA, which is a good solvent for PAA and a poor solvent for PS, is added to promote a less-collapsed star-like PAA core with partially collapsed PS outer blocks.[49] Subsequently, specific amounts of the CFO precursors were added into the solvent mixture under vigorous stirring (see *Experimental section*). The metal precursors were selectively loaded into the compartment occupied by the PAA core due to the strong coordination between the carboxyl groups of PAA blocks and metal moieties of the precursors. Additionally, the poor solubility of the precursors in low-polarity DPE facilitates the precursors to enter into the more polar PAA domains, ensuring the formation of NPs with high yield.

Moreover, after thermolysis, the metal precursors loaded within the space occupied by the PAA core of star-like diblock copolymer nanoreactors were converted into CFO NPs. X-ray diffraction (XRD) analysis confirmed that the CFO spinel structure was successfully formed during thermolysis. A representative diffraction pattern, along with the JCPDS 22-1086 spinel $CoFe_2O_4$ (CFO) standard, is shown in Fig. 1a. As verified by transmission electron microscopy (TEM) imaging, all the yielded colloids consisted of easily distinguishable NPs (Fig. 1b–

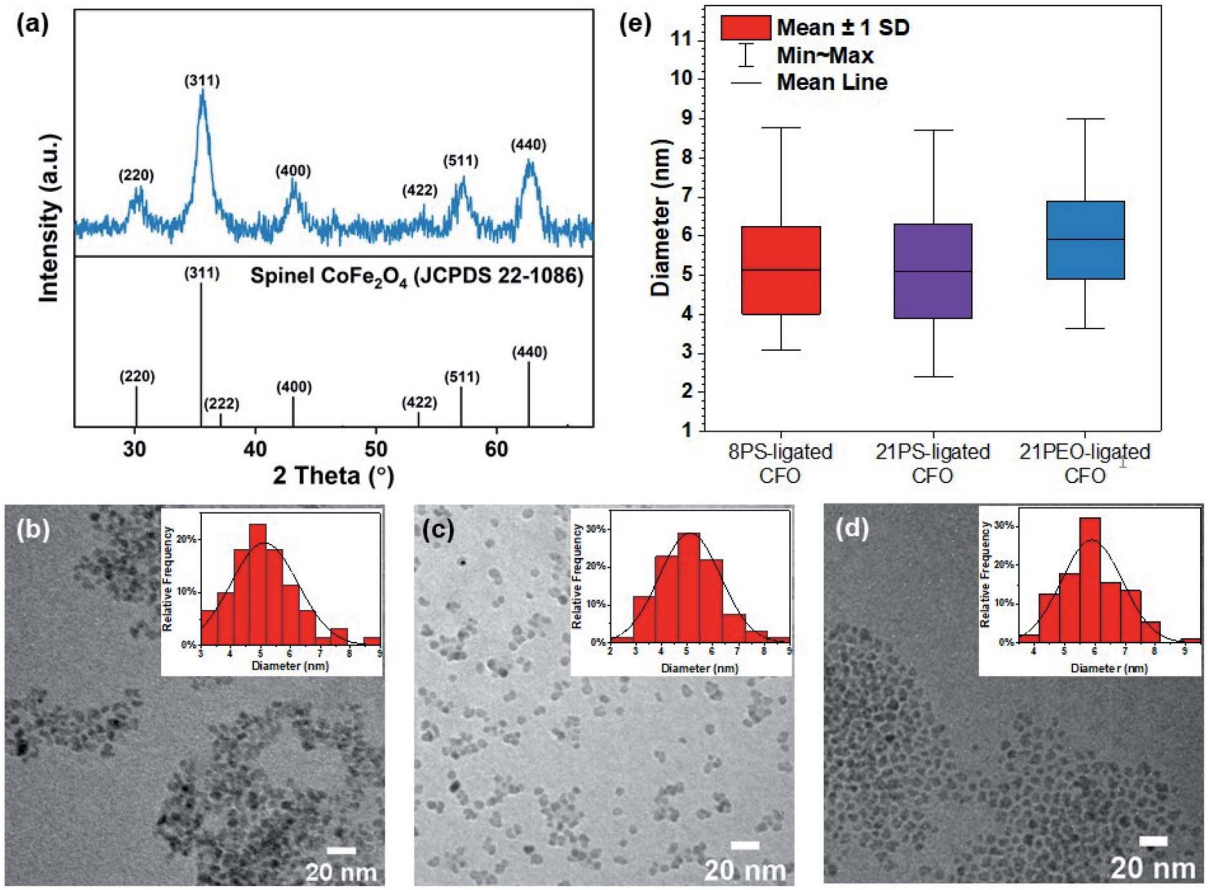

Fig. 1 (a) Representative XRD pattern of the as-synthesized polymer-ligated $CoFe_2O_4$ (CFO) nanoparticles (NPs). TEM images of CFO NPs permanently ligated with (b) 8 PS chains (8PS-ligated CFO), (c) 21 PS chains (21PS-ligated CFO), and (d) 21 PEO chains (21PEO-ligated CFO) with histograms inset. (e) Box and whiskers plot of the diameters of the obtained NPs.

d). Three different sets of CFO NPs were synthesized, that is, CFO intimately and permanently ligated with 8 PS chains (denoted 8PS-ligated CFO) (Fig. 1b), 21 PS chains (denoted 21PS-ligated CFO) (Fig. 1c), and 21 PEO chains (denoted 21PEO-ligated CFO) (Fig. 1d). These NPs had an average diameter of 5.1 ± 1.1 nm, 5.1 ± 1.2 nm, 5.9 ± 1.0 nm, respectively (Fig. 1e). By alternating the composition of the outer blocks from PS to PEO and the grafting density of polymer chains (*i.e.*, 21 arms *vs.* 8 arms), we visualized negligible variation in the size and uniformity of the as-prepared CFO NPs, suggesting only inner PAA blocks determined the size of formed NPs (Table S1†). The produced 8PS-ligated CFO experienced a slightly more aggregation compared to the other NPs, as shown in Fig. 1b. This aggregation can be attributed to the decreased number of polymer chains permanently attached to the CFO surface, which are crucial to the stability of the colloids. To verify the stability of the ligated CFO when exposed to harsh OER conditions, the electrocatalytic activity of 21PS-ligated CFO was measured by linear sweep voltammetry (LSV) prior to and following 100, 300 and 500 cyclic voltammetry (CV) cycles. The 21PS-ligated CFO was found to exhibit high stability, displaying consistent OER activity after 300 cycles (Fig. S9†). While a small increase in η_{10} was observed following 500 CV cycles, this reduction in electrocatalytic performance can be attributed to the detachment of the catalyst layer from the electrode. As the outer blocks (*i.e.*, PS or PEO) are covalently bonded with the inner PAA blocks, they are thereby permanently capped outside the surface of as-prepared CFO NPs without ligand dissociation. As such, our unconventional strategy to craft polymer-ligated CFO NPs of controlled size and tunable surface chemistry enables the exploration of the effect of composition and grafting density on the electrocatalytic performance of CFO NPs as demonstrated below.

2.2 Impact of surface-capping chain density

Due to the surface-reliant nature of electrocatalysis, the impact of the number of permanently capped polymer chains on OER activity was examined. 21PS-ligated CFO and 8PS-ligated CFO electrocatalysts were compared *via* LSV. 8PS-ligated CFO exhibited an η_{10} of 415 mV, outperforming 21PS-ligated CFO which produced an η_{10} of 442 mV (Fig. 2a). Intuitively, this difference in performance is caused by the higher exposed surface area of 8PS-ligated CFO. To verify this, the electrochemically active surface area (ECSA) of both electrocatalysts was gauged by measuring the capacity of their electrochemical double-layers (C_{dl}), which is proportional to the ECSA.[12] The C_{dl}

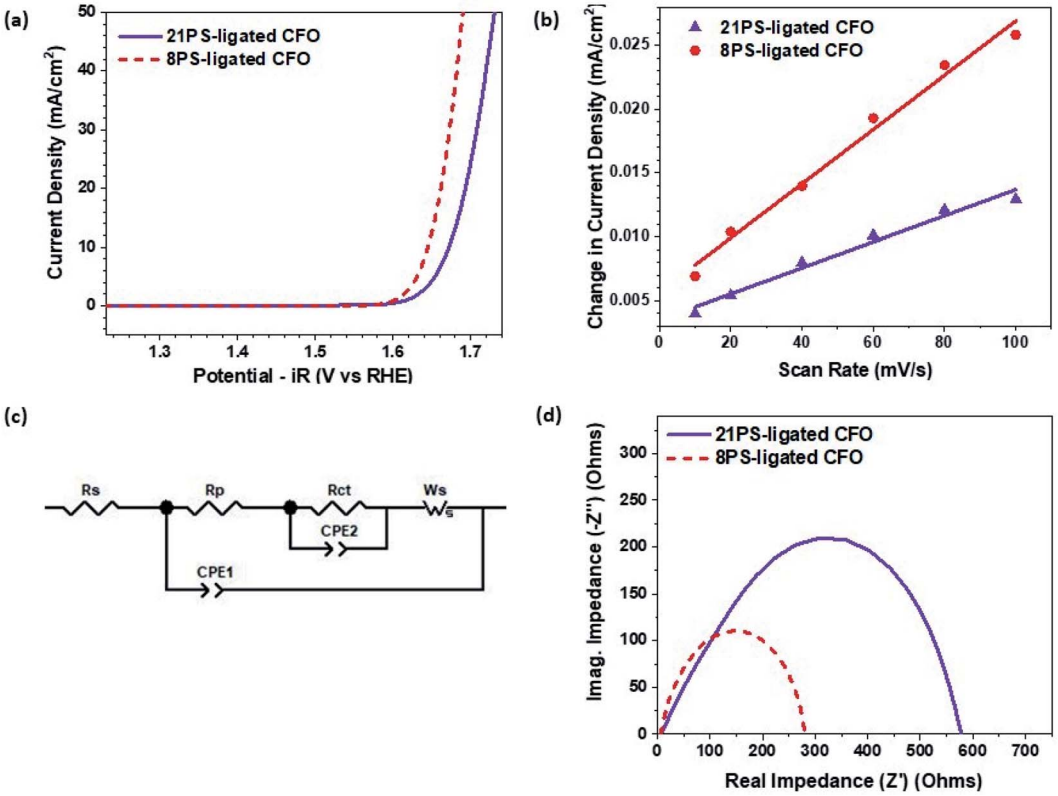

Fig. 2 (a) iR-corrected LSV curves and (b) measured C_{dl}, which is proportional to the ECSA, represented by the slope of the change in current density *vs.* scan rate, of 21PS-ligated CFO and 8PS-ligated CFO in 1 M KOH, O_2-saturated electrolyte. (c) Equivalent circuit for the polymer-ligated CFO electrocatalyst system. (d) EIS Nyquist plots simulated through fitting of the (c) equivalent circuit.

was determined by performing CV scans in a non-faradaic potential range at several different scan rates (Fig. S10†), plotting the measured change in current density against the scan rate, and recording the slope of the resulting linear relationship which is equal to C_{dl}. As shown in Fig. 2b, 8PS-ligated CFO displayed a C_{dl} of 213 μF cm^{-2}, over double that of 21PS-ligated CFO (C_{dl} = 102 μF cm^{-2}), confirming that 8PS-ligated CFO has a higher ECSA and exposed surface area during electrocatalysis.

The increase of OER activity associated with a decrease in the number of polymer arms was further explored *via* electrochemical impedance spectroscopy (EIS). From the Nyquist plots (Fig. S11†), 21PS-ligated CFO displayed a significantly higher total system resistance than 8PS-ligated CFO, producing a semicircle almost twice as large in diameter. The measured EIS data was fit to an equivalent circuit (Fig. 2c), achieving a χ^2 lower than 10^{-3} for both materials, and the full shape of the curves were simulated (Fig. 2d).

The equivalent circuit fit to the measured data comprised several components, including the solution/electrolyte resistance (R_s), pore resistance (R_p), charger-transfer resistance (R_{ct}), two constant phase elements (CPE_1 & CPE_2), and a finite length Warburg element (W_s). Each of these elements are representative of physical phenomena within the electrocatalyst system and their contribution to the overall measured impedance. R_s represents the ohmic internal resistance of the cell, including the solution/electrolyte resistance and the resistance of the electrodes. R_{ct} reflects the charge-transfer resistance of the active material, namely CFO in this system, and R_p is the resistance of the pores created by the polymer chains surrounding the CFO NP. CPE_1 and CPE_2 represent the C_{dl} of the pores created by the polymer chains and the active material (CFO), respectively; constant phase elements are used in place of capacitor elements due to the well-established frequency dependence of the measured electrode–electrolyte interfacial capacitance.[51] Lastly, W_s is the diffusion related impedance in the system, where a typical Warburg element behavior (45° slope) is present at high frequencies but does not continue through lower frequencies; this behavior is typical for RDEs.[52] The W_s element depends on three parameters, R_W, T_W and P_W, which relate to the W_s impedance (Z_W) as shown in eqn (1).[53]

$$Z_W = R_W n \frac{\tan h\left[(jT_W\omega)^{P_W}\right]}{(jT_W\omega)^{P_W}} \quad (1)$$

where R_W represents diffusion resistance, P_W is an exponent set to 0.5 so eqn (1) is the solution of the one-dimensional diffusion equation of a particle, and T_W is defined by eqn (2).[40]

$$T_W = L^2/D \quad (2)$$

where L is the effective diffusion thickness and D is the effective diffusion n coefficient of the particle.

Based on the equivalent circuit fitting of the EIS curves, the most significant differences between the two materials stem from their R_p, R_W, and T_W components (Table S2†). 21PS-ligated CFO exhibited a R_p of 0.8 Ω, while 8PS-ligated CFO contrastingly exhibited a R_p so small that it approached 0 Ω; a higher R_p indicates that the pores of 21PS-ligated CFO have smaller diameters and/or longer lengths than 8PS-ligated CFO pores.[54] Additionally, 21PS-ligated CFO displayed much higher R_W (350 Ω) and T_W (2.8) in comparison to 8PS-ligated CFO (R_W = 80 Ω, T_W = 0.012), suggesting that the decrease of polymer arms drastically reduced the diffusion resistance of the system.

Therefore, the observed increase in OER activity associated with a decrease in the number of surface-capping polymer chains is ascribed to two different factors. First, fewer chains on the NP surface allow the electrolyte easier access to the active electrocatalyst material, CFO, as suggested by the increased ECSA and decreased R_P. Second, by utilizing only 8 PS chains instead of 21, the space surrounding the CFO NPs becomes less crowded, significantly lowering the diffusion resistance and effective diffusion thickness in the material system.

2.3 Influence of surface-capping chain hydrophilicity

As electrolysis occurs in a water-based electrolyte, it is imperative to determine the impact of the surface-capping chain hydrophilicity on the overall activity of the electrocatalysts. The OER activity of CFO NPs ligated with 21 PS chains (21PS-ligated CFO), which are hydrophobic, and CFO NPs ligated with 21 PEO chains (21PEO-ligated CFO), which are hydrophilic, were compared. 21PEO-ligated CFO outperformed 21PS-ligated CFO, exhibiting an η_{10} of 409 mV and 442 mV, respectively, as measured by LSV (Fig. 3a).

To further investigate the observed difference in OER activity, EIS was utilized to gain insight into the electronic behavior of the catalysts. From the Nyquist plots (Fig. S12†), 21PS-ligated CFO displayed a significantly higher total system resistance than 21PEO-ligated CFO, producing a semicircle approximately 400 Ω larger in diameter. The measured EIS data was fit to the same equivalent circuit utilized previously (Fig. 2c), again achieving a χ^2 lower than 10^{-3}, and the full shape of the curves were simulated (Fig. 3c). Based on the equivalent circuit fitting of the EIS curves, the most significant differences between the two materials stem from their R_p, R_{ct}, R_W, and T_W components (Table S2†). Unexpectedly, 21PEO-ligated CFO exhibited a larger R_p (1.9 Ω) than 21PS-ligated CFO (R_p = 0.8 Ω). Although surprising, this increased R_p accounts for the more distinctive high-frequency semicircle that appears in the 21PEO-ligated CFO Nyquist plot (Fig. 3c), further supporting the accuracy of the equivalent circuit fit. In contrast, 21PS-ligated CFO displayed a significantly larger R_{ct} (220 Ω), R_W (350 Ω) and T_W (2.8) compared to 21PEO-ligated CFO (R_{ct} = 130 Ω, R_W = 20 Ω, T_W = 0.23).

The measured increase in OER activity associated with an increase in surface-capping chain hydrophilicity is ascribed to

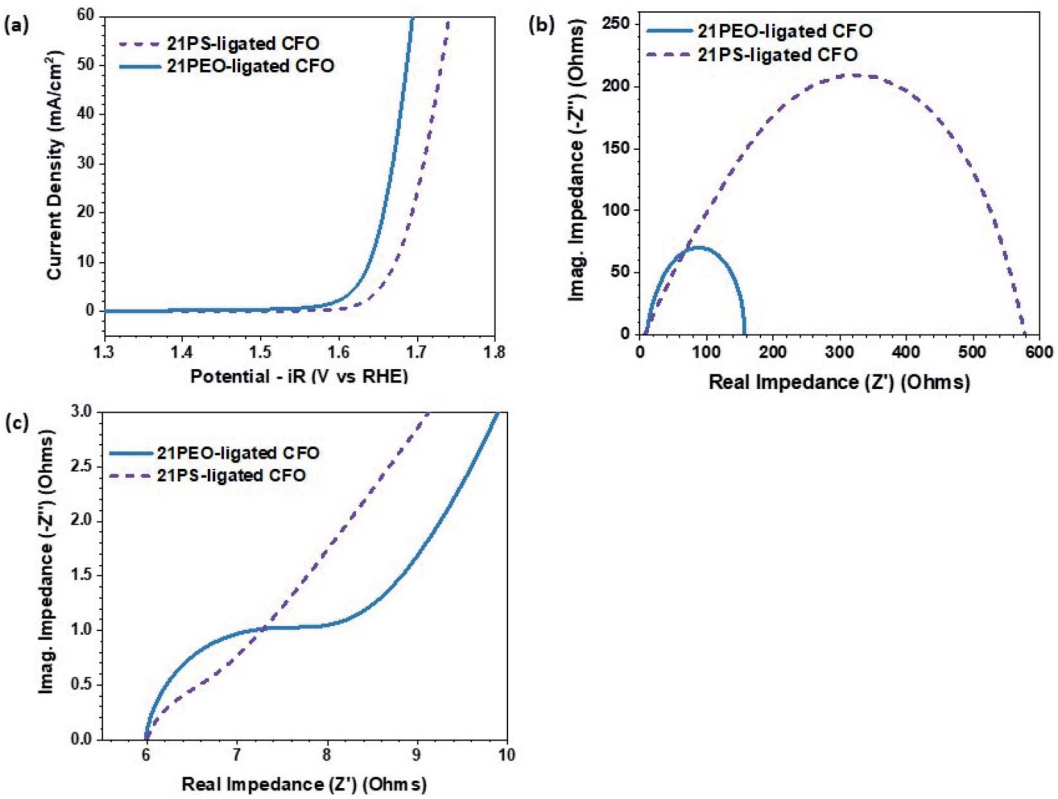

Fig. 3 (a) LSV curves and (b) EIS Nyquist plots of 21PS-ligated CFO and 21PEO-ligated CFO in 1 M KOH, O_2-saturated electrolyte, inset: equivalent circuit. (c) Zoomed-in graph of EIS Nyquist plot in (b).

two different factors. First, the tendency of more hydrophilic polymers to expand in the water-based electrolyte exposes more of the CFO surface to the electrolyte as suggested by the significantly decreased R_{ct} observed. In addition, as the PEO chains prefer polymer–electrolyte interactions over polymer–polymer interactions,[55] the surface-ligating chains expand in the electrolyte, providing larger channels for diffusion of reactants/products to/from the electrocatalyst surface to occur through as suggested by the large decrease in R_W and T_W.

2.4 Correlation between surface-capping chain behavior and electrocatalytic performance

Through the investigation of surface-capping polymer properties and their impact on the OER activity of polymer-ligated CFO NPs, it was determined that changes in the diffusion resistance of the system and exposure of the active material to the electrolyte had the largest effect on electrocatalytic behavior. Decreasing the number of polymer chains and increasing the hydrophilicity of the outer-block chains of the synthesized star-like diblock copolymer both resulted in significantly increased OER performance. Thus, the results from the surface-capping chain density and hydrophilicity tests were scrutinized to provide insight into the physical phenomena occurring within the polymer-ligated NP system responsible for the notable electrocatalytic differences.

Due to their hydrophobic nature, PS chains collapse once in contact with the electrolyte. It is proposed that the collapse of PS chains on the electrocatalyst surface forms an effective porous polymer shell, and the size of the pore channels within the shell is the limiting factor for OER activity. From the collected LSV data (Fig. 2a and **3a**), it was determined that OER activity of the samples followed the trend: 21PS-ligated CFO < 8PS-ligated CFO < 21PEO-ligated CFO (η_{10} = 409 mV < 415 mV < 442 mV). Therefore, the pore channel size within the polymer shells should follow the opposite trend, with 21PS-ligated CFO having the smallest pore channels and 21PEO-ligated CFO having the largest.

As determined by fitting the measured EIS data to an equivalent circuit (Fig. 2c), ~61% of the overall resistance for the 21PS-ligated CFO system can be attributed to diffusion resistance (R_W = 350 Ω) (Table S2†). Additionally, a small, distinct semicircle is present at high frequency in the corresponding Nyquist plot (Fig. S12; inset†), which was ascribed to the impedance contribution from a porous coating/shell. Taken together, these two observations suggest that the collapsed PS chains form a porous shell around CFO, containing small pore channels through which electrolyte travels to interact with the NP surface, as illustrated in Fig. 4 (upper panel).

By capping CFO with fewer polymer chains, several changes in the catalyst electrochemistry occurred. 8PS-ligated CFO exhibited a C_{dl} over twice that of 21PS-ligated CFO (Fig. 2b), meaning that the exposure of the NP surface to the electrolyte is significantly higher. The pore resistance of the 8PS-ligated CFO nearly approaches zero, and, in contrast to 21PS-ligated CFO, there is no presence of a high frequency semicircle in the Nyquist plot (Fig. S11; inset†). Nevertheless, while remarkably lower, the diffusion resistance (R_W = 80 Ω) still accounts for ~29% of the overall resistance for the 8PS-ligated CFO system. These findings signify that 8PS-ligated CFO contains wider, shorter pore channels in comparison to 21PS-ligated CFO (Fig. 4; lower right panel).

Utilizing hydrophilic outer-block chains, the diffusion resistance (R_W) of 21PEO-ligated CFO was measured to be just 20 Ω (Table S2†), which only comprises ~13% of the total system resistance. Additionally, 21PEO-ligated CFO displayed a greatly lower R_{ct} of 130 Ω compared to 21PS-ligated CFO (R_{ct} = 220 Ω) and 8PS-ligated CFO (R_{ct} = 190 Ω), indicative of a much

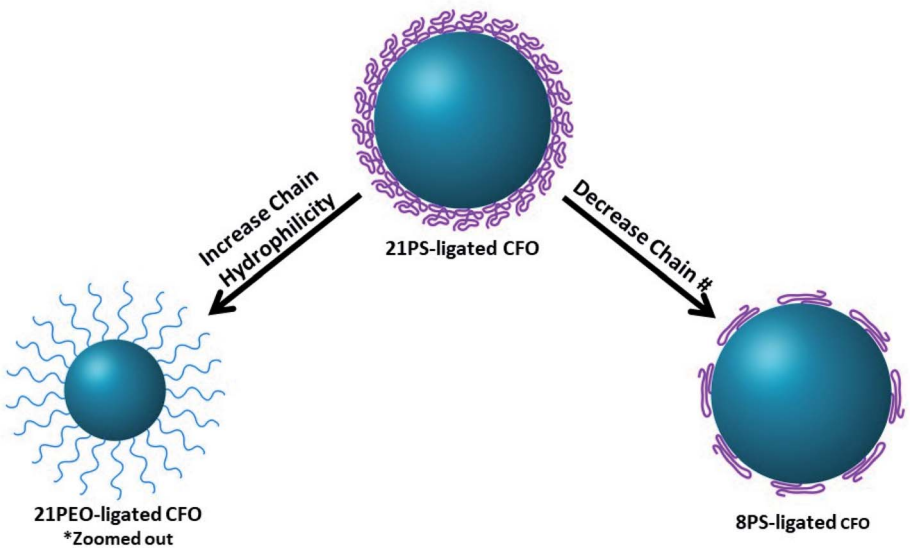

Fig. 4 Schematic illustration of proposed scenarios with the outer polymer chains forming an effective porous shell surrounding CFO NPs, accounting for the difference in OER performance of the respective polymer-ligated CFO NPs. Decreasing the number of outer polymer chains or increasing their hydrophilicity results in the increase of the pore channel size.

higher exposure of the NP surface to electrolyte, which can be rationalized due to wider pore channels in the polymer shell. 21PEO-ligated CFO was found to manifest a larger, more distinct high frequency semicircle in the Nyquist plot (Fig. 3c) and considerably increased pore resistance ($R_P = 1.9\ \Omega$). This increased R_P resulted from the expanded hydrophilic PEO chains, which create markedly longer pore channels. These results reveal that 21PEO-ligated CFO contains longer and notably broader pore channels in comparison to 21PS-ligated CFO (Fig. 4; lower left panel).

3. Conclusions

In summary, we crafted CFO NPs permanently ligated with 8 PS, 21 PS or 21 PEO chains, *via* employing rationally designed star-like diblock copolymers as nanoreactors, and scrutinized the effects of chain grafting density and hydrophilicity on the OER activity of CFO NPs. The comparison of the electrochemical and electrocatalytic properties of the three types of polymer-ligated CFO NPs revealed that both the number of surface polymer chains and their hydrophilicity exerted a significant impact on OER activity. As the number of surface-capping polymer chains decreased from 21 to 8, a 21 mV decrease of η_{10} was observed, which was attributed to the corresponding increase of ECSA and drastic decrease of diffusion resistance. It was found that hydrophilic surface-capping polymers resulted in greatly enhanced OER activity over hydrophobic polymers, yielding a 33 mV decrease in η_{10}. A marked decrease in R_{ct} and diffusion resistance was determined as the cause of the improved electrocatalytic performance. The corresponding decrease of diffusion resistance seen in these cases is proposed to be a result of the enlargement of pore channels within the effective polymer shells formed by the outer-block chains permanently capping CFO NPs. Our study suggests that the negative impact of surface-capping polymers on electrocatalysis can be reduced by regulating the surface-capping polymer properties, especially the number of capping chains and their hydrophilicity. By mitigating this negative impact, surface polymers carry the potential to be effectively employed for stabilizing NPs in electrocatalysis. This work opens the perspective for future systematic research regarding the judicious tuning of surface chemistry tuning of polymer-ligated NPs to further tailor and/or enhance electrocatalytic performance of NPs.

Conflicts of interest

There are no conflicts to declare.

Acknowledgements

This work is supported by the AFOSR (FA9550-19-1-0317).

References

1 N. S. Lewis and D. G. Nocera, Powering the planet: Chemical challenges in solar energy utilization, *Proc. Natl. Acad. Sci. U. S. A.*, 2006, **103**(43), 15729–15735.
2 V. R. Stamenkovic, D. Strmcnik, P. P. Lopes and N. M. Markovic, Energy and fuels from electrochemical interfaces, *Nat. Mater.*, 2017, **16**(1), 57–69.
3 S. Chu, Y. Cui and N. Liu, The path towards sustainable energy, *Nat. Mater.*, 2017, **16**(1), 16–22.
4 A. Manikandan, P. R. Ilango, C. W. Chen, Y. C. Wang, Y. C. Shih, L. Lee, Z. M. M. Wang, H. Ko and Y. L. Chueh, A superior dye adsorbent towards the hydrogen evolution reaction combining active sites and phase-engineering of (1T/2H) MoS2/-MoO3 hybrid heterostructured nanoflowers, *J. Mater. Chem. A*, 2018, **6**(31), 15320–15329.
5 J. Sun, N. Guo, Z. Shao, K. Huang, Y. Li, F. He and Q. Wang, A Facile Strategy to Construct Amorphous Spinel-Based Electrocatalysts with Massive Oxygen Vacancies Using Ionic Liquid Dopant, *Adv. Energy Mater.*, 2018, **8**(27), 1–13.
6 Y. Li and H. Dai, Recent advances in zinc-air batteries, *Chem. Soc. Rev.*, 2014, **43**(15), 5257–5275.
7 G. Wan, P. Yu, H. Chen, J. Wen, C.-j. Sun, H. Zhou, N. Zhang, Q. Li, W. Zhao, B. Xie, T. Li and J. Shi, Engineering Single-Atom Cobalt Catalysts toward Improved Electrocatalysis, *Small*, 2018, **14**(15), 1704319.
8 B.-Q. Li, C.-X. Zhao, S. Chen, J.-N. Liu, X. Chen, L. Song and Q. Zhang, Framework-Porphyrin-Derived Single-Atom Bifunctional Oxygen Electrocatalysts and their Applications in Zn-Air Batteries, *Adv. Mater.*, 2019, **31**(19), 1–8.
9 H. Zhang, G. Liu, L. Shi and J. Ye, Single-Atom Catalysts: Emerging Multifunctional Materials in Heterogeneous Catalysis, *Adv. Energy Mater.*, 2018, **8**(1), 1–24.
10 X. Zhang, Y. F. Zhao, Y. X. Zhao, R. Shi, G. I. N. Waterhouse and T. R. Zhang, A Simple Synthetic Strategy toward Defect-Rich Porous Monolayer NiFe-Layered Double Hydroxide Nanosheets for Efficient Electrocatalytic Water Oxidation, *Adv. Energy Mater.*, 2019, **9**(24), 1900881.
11 Y. Wang, Y. Zhang, Z. Liu, C. Xie, S. Feng, D. Liu, M. Shao and S. Wang, Layered Double Hydroxide Nanosheets with Multiple Vacancies Obtained by Dry Exfoliation as Highly Efficient Oxygen Evolution Electrocatalysts, *Angew. Chem., Int. Ed.*, 2017, **56**(21), 5867–5871.
12 T. Li, Y. Lv, J. Su, Y. Wang, Q. Yang, Y. Zhang, J. Zhou, L. Xu, D. Sun and Y. Tang, Anchoring CoFe2O4 Nanoparticles on N-Doped Carbon Nanofibers for High-Performance Oxygen Evolution Reaction, *Adv. Sci.*, 2017, **4**(11), 1700226.
13 X. Ge, A. Sumboja, D. Wuu, T. An, B. Li, F. W. T. Goh, T. S. A. Hor, Y. Zong and Z. Liu, Oxygen Reduction in Alkaline Media: From Mechanisms to Recent Advances of Catalysts, *ACS Catal.*, 2015, **5**(8), 4643–4667.
14 A. Alarawi, V. Ramalingam and J. H. He, Recent advances in emerging single atom confined two-dimensional materials for water splitting applications, *Mater. Today Energy*, 2019, **11**, 1–23.
15 S. Kattel, P. Atanassov and B. Kiefer, Catalytic activity of Co-N-x/C electrocatalysts for oxygen reduction reaction: a density functional theory study, *Phys. Chem. Chem. Phys.*, 2013, **15**(1), 148–153.
16 N.-T. Suen, S.-F. Hung, Q. Quan, N. Zhang, Y.-J. Xu and H. M. Chen, Electrocatalysis for the oxygen evolution

reaction: recent development and future perspectives, *Chem. Soc. Rev.*, 2017, **46**(2), 337–365.
17 X. Sun, L. F. Gao, C. Y. Guo, Y. Zhang, X. Kuang, T. Yan, L. Ji and Q. Wei, Sulfur Incorporated CoFe2O4/Multiwalled Carbon Nanotubes toward Enhanced Oxygen Evolution Reaction, *Electrochim. Acta*, 2017, **247**, 843–850.
18 Y. L. Niu, X. Q. Huang, L. Zhao, W. H. Hu and C. M. Li, One-Pot Synthesis of Co/CoFe2O4 Nanoparticles Supported on N-Doped Graphene for Efficient Bifunctional Oxygen Electrocatalysis, *ACS Sustainable Chem. Eng.*, 2018, **6**(3), 3556–3564.
19 X. Zou and Y. Zhang, Noble metal-free hydrogen evolution catalysts for water splitting, *Chem. Soc. Rev.*, 2015, **44**(15), 5148–5180.
20 C. Wu, J. Zhang, X. Tong, P. Yu, J. Y. Xu, J. Wu, Z. M. M. Wang, J. Lou and Y. L. Chueh, A Critical Review on Enhancement of Photocatalytic Hydrogen Production by Molybdenum Disulfide: From Growth to Interfacial Activities, *Small*, 2019, **15**(35), 1900578.
21 Y. Tang and W. Cheng, Key parameters governing metallic nanoparticle electrocatalysis, *Nanoscale*, 2015, **7**(39), 16151–16164.
22 X. Pang, L. Zhao, C. Feng and Z. Lin, Novel Amphiphilic Multiarm, Starlike Coil-Rod Diblock Copolymers via a Combination of Click Chemistry with Living Polymerization, *Macromolecules*, 2011, **44**(18), 7176–7183.
23 J. C. Meier, I. Katsounaros, C. Galeano, H. J. Bongard, A. A. Topalov, A. Kostka, A. Karschin, F. Schueth and K. J. J. Mayrhofer, Stability investigations of electrocatalysts on the nanoscale, *Energy Environ. Sci.*, 2012, **5**(11), 9319–9330.
24 X. D. Jia, X. Zhang, J. Q. Zhao, Y. F. Zhao, Y. X. Zhao, G. I. N. Waterhouse, R. Shi, L. Z. Wu, C. H. Tung and T. R. Zhang, Ultrafine monolayer Co-containing layered double hydroxide nanosheets for water oxidation, *J. Energy Chem.*, 2019, **34**, 57–63.
25 A. Alarawi, V. Ramalingam, H. C. Fu, P. Varadhan, R. S. Yang and J. H. He, Enhanced photoelectrochemical hydrogen production efficiency of MoS2-Si heterojunction, *Opt. Express*, 2019, **27**(8), A352–A363.
26 T. Murase, H. Irie and K. Hashimoto, Visible light sensitive photocatalysts, nitrogen-doped Ta2O5 powders, *J. Phys. Chem. B*, 2004, **108**(40), 15803–15807.
27 M. Zhang, X. Yang, X. Kan, X. Wang, L. Ma and M. Jia, Carbon-encapsulated CoFe2O4/graphene nanocomposite as high performance anode for lithium ion batteries, *Electrochim. Acta*, 2013, **112**, 727–734.
28 L. F. Pan, Y. H. Li, S. Yang, P. F. Liu, M. Q. Yu and H. G. Yang, Molybdenum carbide stabilized on graphene with high electrocatalytic activity for hydrogen evolution reaction, *Chem. Commun.*, 2014, **50**(86), 13135–13137.
29 D. C. B. Alves, R. Silva, D. Voiry, T. Asefa and M. Chhowalla, Copper nanoparticles stabilized by reduced graphene oxide for CO2 reduction reaction, *Mater. Renew. Sustain. Energ.*, 2015, **4**(1), 1–7.
30 Y. Chen, S. Xu, Y. Li, R. J. Jacob, Y. Kuang, B. Liu, Y. Wang, G. Pastel, L. G. Salamanca-Riba, M. R. Zachariah and L. Hu, FeS2 Nanoparticles Embedded in Reduced Graphene Oxide toward Robust, High-Performance Electrocatalysts, *Adv. Energy Mater.*, 2017, **7**(19), 1700482.
31 X. Tuaev, J. P. Paraknowitsch, R. Illgen, A. Thomas and P. Strasser, Nitrogen-doped coatings on carbon nanotubes and their stabilizing effect on Pt nanoparticles, *Phys. Chem. Chem. Phys.*, 2012, **14**(18), 6444–6447.
32 Y. Lu, D. Q. Fan, Z. P. Chen, W. P. Xiao, C. C. Cao and X. F. Yang, Anchoring Co3O4 nanoparticles on MXene for efficient electrocatalytic oxygen evolution, *Sci. Bull.*, 2020, **65**(6), 460–466.
33 A. Manikandan, L. Lee, Y. C. Wang, C. W. Chen, Y. Z. Chen, H. Medina, J. Y. Tseng, Z. M. M. Wang and Y. L. Chueh, Graphene-coated copper nanowire networks as a highly stable transparent electrode in harsh environments toward efficient electrocatalytic hydrogen evolution reactions, *J. Mater. Chem. A*, 2017, **5**(26), 13320–13328.
34 M. S. Jahan, *ESR Insights into Macroradicals in UHMWPE*, 2016, pp. 668–692.
35 K. C. Kwon, J. M. Suh, R. S. Varma, M. Shokouhimehr and H. W. Jang, Electrocatalytic Water Splitting and CO2 Reduction: Sustainable Solutions via Single-Atom Catalysts Supported on 2D Materials, *Small Methods*, 2019, **3**(9), 1800492.
36 X. Cui, Y. Chen, M. Zhang, Y. W. Harn, J. Qi, L. Gao, Z. L. Wang, J. Huang, Y. Yang and Z. Lin, Tailoring carrier dynamics in perovskite solar cells via precise dimension and architecture control and interfacial positioning of plasmonic nanoparticles, *Energy Environ. Sci.*, 2020, **13**(6), 1743–1752.
37 D. K. Pattadar and F. P. Zamborini, Size Stability Study of Catalytically Active Sub-2 nm Diameter Gold Nanoparticles Synthesized with Weak Stabilizers, *J. Am. Chem. Soc.*, 2018, **140**(43), 14126–14133.
38 Y. Liang, Y. Li, H. Wang, J. Zhou, J. Wang, T. Regier and H. Dai, Co3O4 nanocrystals on graphene as a synergistic catalyst for oxygen reduction reaction, *Nat. Mater.*, 2011, **10**(10), 780–786.
39 M. Grzelczak, J. Zhang, J. Pfrommer, J. Hartmann, M. Driess, M. Antonietti and X. Wang, Electro- and Photochemical Water Oxidation on Ligand-free Co3O4 Nanoparticles with Tunable Sizes, *ACS Catal.*, 2013, **3**(3), 383–388.
40 Z. S. Yang and J. J. Wu, Pd/Co Bimetallic Nanoparticles: Coelectrodeposition under Protection of PVP and Enhanced Electrocatalytic Activity for Ethanol Electrooxidation, *Fuel Cells*, 2012, **12**(3), 420–425.
41 D. Li, C. Wang, D. Tripkovic, S. Sun, N. M. Markovic and V. R. Stamenkovic, Surfactant Removal for Colloidal Nanoparticles from Solution Synthesis: The Effect on Catalytic Performance, *ACS Catal.*, 2012, **2**(7), 1358–1362.
42 L. Nguyen Viet, M. Ohtaki, M. Nogami and H. Tong Duy, Effects of heat treatment and poly(vinylpyrrolidone) (PVP) polymer on electrocatalytic activity of polyhedral Pt nanoparticles towards their methanol oxidation, *Colloid Polym. Sci.*, 2011, **289**(12), 1373–1386.
43 Y. Lu, Y. Wang and W. Chen, Silver nanorods for oxygen reduction: Strong effects of protecting ligand on the

electrocatalytic activity, *J. Power Sources*, 2011, **196**(6), 3033–3038.

44 G. Ou, F. C. Wu, K. Huang, N. Hussain, D. Zu, H. H. Wei, B. H. Ge, H. Z. Yao, L. Liu, H. N. Li, Y. M. Shi and H. Wu, Boosting the Electrocatalytic Water Oxidation Performance of CoFe2O4 Nanoparticles by Surface Defect Engineering, *ACS Appl. Mater. Interfaces*, 2019, **11**(4), 3978–3983.

45 X. F. Lu, L. F. Gu, J. W. Wang, J. X. Wu, P. Q. Liao and G. R. Li, Bimetal-Organic Framework Derived CoFe2O4/C Porous Hybrid Nanorod Arrays as High-Performance Electrocatalysts for Oxygen Evolution Reaction, *Adv. Mater.*, 2017, **29**(3), 1604437.

46 X. Pang, L. Zhao, M. Akinc, J. K. Kim and Z. Lin, Novel Amphiphilic Multi-Arm, Star-Like Block Copolymers as Unimolecular Micelles, *Macromolecules*, 2011, **44**(10), 3746–3752.

47 X. Pang, L. Zhao, W. Han, X. Xin and Z. Lin, A general and robust strategy for the synthesis of nearly monodisperse colloidal nanocrystals, *Nat. Nanotechnol.*, 2013, **8**(6), 426–431.

48 Y. He, Y. J. Yoon, Y. W. Harn, G. V. Biesold-McGee, S. Liang, C. H. Lin, V. V. Tsukruk, N. Thadhani, Z. Kang and Z. Lin, Unconventional route to dual-shelled organolead halide perovskite nanocrystals with controlled dimensions, surface chemistry, and stabilities, *Sci. Adv.*, 2019, **5**(11), eaax4424.

49 L. Gao, X. Cui, Z. Wang, C. D. Sewell, Z. Li, S. Liang, M. Zhang, J. Li, Y. Hu and Z. Lin, Operando unraveling photothermal-promoted dynamic active-sites generation in NiFe2O4 for markedly enhanced oxygen evolution, *Proc. Natl. Acad. Sci. U. S. A.*, 2021, **118**(7), e2023421118.

50 Y. Liu, J. Wang, M. Zhang, H. Li and Z. Lin, Polymer-Ligated Nanocrystals Enabled by Nonlinear Block Copolymer Nanoreactors: Synthesis, Properties, and Applications, *ACS Nano*, 2020, **14**(10), 12491–12521.

51 R. K. Singh, R. Devivaraprasad, T. Kar, A. Chakraborty and M. Neergat, Electrochemical Impedance Spectroscopy of Oxygen Reduction Reaction (ORR) in a Rotating Disk Electrode Configuration: Effect of Ionomer Content and Carbon-Support, *J. Electrochem. Soc.*, 2015, **162**(6), F489–F498.

52 T. Jacobsen and K. West, Diffusion Impedance In Planar, Cylindrical And Spherical-Symmetry, *Electrochim. Acta*, 1995, **40**(2), 255–262.

53 D. Johnson, *ZView Impedance/Gain Phase Graphing and Analysis Software Operating Manual, 3.5*, Scribner Associates, Inc.: Southern Pines, NC, 2019.

54 K. Kant, C. Priest, J. G. Shapter and D. Losic, The Influence of Nanopore Dimensions on the Electrochemical Properties of Nanopore Arrays Studied by Impedance Spectroscopy, *Sensors*, 2014, **14**(11), 21316–21328.

55 U. Dahal and E. E. Dormidontova, Chain Conformation and Hydration of Polyethylene Oxide Grafted to Gold Nanoparticles: Curvature and Chain Length Effect, *Macromolecules*, 2020, **53**(19), 8160–8170.

